Materials Today Bio 15 (2022) 100274

Contents lists available at ScienceDirect

Materials Today Bio

journal homepage: www.journals.elsevier.com/materials-today-bio

Ordered micropattern arrays fabricated by lung-derived dECM hydrogels for chemotherapeutic drug screening

Xinglong Zhu [a,1], Yi Li [b,c,1], Ying Yang [b,c], Yuting He [a], Mengyu Gao [a], Wanliu Peng [a], Qiong Wu [a], Guangyue Zhang [d], Yanyan Zhou [a], Fei Chen [a], Ji Bao [a,*], Weimin Li [b,c,e,**]

[a] Institute of Clinical Pathology, Key Laboratory of Transplant Engineering and Immunology, NHC, West China Hospital, Sichuan University, Chengdu, 610041, Sichuan, China
[b] Institute of Respiratory Health, West China Hospital, Sichuan University, Chengdu, 610041, Sichuan, China
[c] Precision Medicine Key Laboratory, West China Hospital, Sichuan University, Chengdu, 610041, Sichuan, China
[d] West China School of Medicine, Sichuan University, Chengdu, 610041, Sichuan, China
[e] Department of Respiratory and Critical Care Medicine, West China Hospital, Sichuan University, Chengdu, 610041, China

ARTICLE INFO

Keywords:
Extracellular matrix
Lung
Decellularization
Cancer cell
Drug screening

ABSTRACT

Aims: This study aims to evaluate ECM-coated micropattern arrays derived from decellularization of native porcine lungs as a novel three-dimensional cell culture platform.
Methods: ECM derived from decellularization of native porcine lungs was exploited to prepare hydrogels. Then, dECM-coated micropattern arrays were fabricated at four different diameters (50, 100, 150 and 200 μm) using polydimethylsiloxane (PDMS). Two lung cancer cell lines, A549 and H1299, were tested on a dECM-coated micropattern array as a novel culture platform for cell adhesion, distribution, proliferation, viability, phenotype expression, and drug screening to evaluate the cytotoxicity of paclitaxel, doxorubicin and cisplatin.
Results: The ECM derived from decellularization of native porcine lungs supported cell adhesion, distribution, viability and proliferation better than collagen I and Matrigel as the coated matrix on the surface. Moreover, the optimal diameter of the micropattern arrays was 100–150 μm, as determined by measuring the morphology, viability, proliferation and phenotype of the cancer cell spheroids. Cell spheroids of A549 and H1299 on dECM-coated micropattern arrays showed chemoresistance to anticancer drugs compared to that of the monolayer. The different distributions of HIF-1α, MCL-1 (in the center) and Ki-67 and MRP2 (in the periphery) of the spheroids demonstrated the good establishment of basal-lateral polarity and explained the chemoresistance phenomenon of spheroids.
Conclusions: This novel three-dimensional cell culture platform is stable and reliable for anticancer drug testing. Drug screening in dECM-coated micropattern arrays provides a powerful alternative to existing methods for drug testing and metabolic profiling in the drug discovery process.

1. Introduction

Traditionally, anticancer drugs are evaluated in conventional two-dimensional cell culture platforms (monolayers), such as growing cells on polystyrene dishes. However, conventional two-dimensional cultured cancer cells cannot mimic the complexity of cell–cell and cell-matrix interactions or the heterogeneity of tumors, which usually grow in a three-dimensional conformation *in vivo* [1]. Thus, the results of efficacy and cytotoxicity assays often exhibit differences from those of animal studies and human trials, leading to the failure of new drugs in clinical trials. To overcome this, several techniques are currently being developed that can mimic the microenvironment as spheroids or organoids to rebuild the interaction signals for cell survival, proliferation, differentiation, and gene expression. Recent three-dimensional cell culture models narrow the gap between two-dimensional cell culture models and animal disease models by mimicking the realistic microenvironment of cell–cell

* Corresponding author. Institute of Clinical Pathology, West China Hospital, Sichuan University, 37# Guoxue Road, Chengdu, 610041, Sichuan Province, China.
** Corresponding author. Department of Respiratory and Critical Care Medicine, West China Hospital, Sichuan University, 37# Guoxue Road, Chengdu 610041, Sichuan Province, China.
E-mail addresses: baoji@scu.edu.cn (J. Bao), weimi003@scu.edu.cn (W. Li).
[1] The authors contributed equally to this work.

https://doi.org/10.1016/j.mtbio.2022.100274
Received 12 February 2022; Received in revised form 25 April 2022; Accepted 26 April 2022
Available online 5 May 2022

and cell-matrix and recapitulating natural three-dimensional tumors [2,3]. They are also useful in drug discovery for determining the sensitivity of chemotherapeutics to tumor cells at both the cellular and molecular levels.

The presence of an intact native extracellular matrix (ECM) is of central importance, as it not only provides a platform for cell growth, proliferation, differentiation, polarization, migration and organization but is also thought to mediate biochemical and molecular signaling, such as neovascularization and cancer progression [4,5]. The matrix scaffold acquired from decellularization of donor organs holds great potential for maintaining the composition of ECM. Key proteins, such as collagen, fibronectin, and laminin, as well as activated growth factors and cytokines are well preserved after decellularization derived from native organs [6,7]. Recently, lung dECM hydrogels derived from healthy and diseased lungs have been further developed as a model to study ECM with similar mechanical properties [8]. Besides, dECM can also serve as coating [9] and embedding [10], bioink for three-dimensional culture [11,12], and injectable biological scaffolds to protect against radiation lung injury [13]. Decellularized ECM-based hydrogels are therefore particularly gaining attention due to their property and perfect homogeneity [6,14,15]. Moreover, natural-synthetic polymer hydrogels have also been proposed to construct ideal bionic tissues and sophisticated structures [16,17].

Another obstacle that must be overcome is to standardize and control the size and arrangement of spheroids or organoids, which could strongly affect drug efficacy and toxicity [18], as currently common three-dimensional cultures will not be able to be repeatedly and accurately measured [2]. Advances have been made on this front to standardize the concordance of spheroid morphological characteristics to reduce heterogeneity and increase reproducibility. Micropattern arrays form a patterned arrangement of defined shape and size on planar substrates by covalently or noncovalently coating carbohydrates, peptides and proteins, thus offering the advantage of culturing cells at high throughput, increasing functionality and improving uniformity at the same time [19,20]. For example, polydimethylsiloxane (PDMS) is widely used in the fields of cytology, drug screening and tissue engineering to create specific micropattern arrays of proteins on nonattachment plates [19,21].

In this study, we exploited ECM derived from decellularization of native porcine lungs to prepare hydrogels. The characteristics of dECM-based hydrogels were measured and compared with traditional coating substrates, including collagen I and Matrigel. Furthermore, we explored the fabrication of dECM-coated micropattern arrays at different diameters (50, 100, 150 and 200 μm) using PDMS. Two lung cancer cell lines, A549 and H1299, were tested on our dECM-coated micropattern array as a novel culture platform for drug screening to evaluate the cytotoxicity of paclitaxel, doxorubicin and cisplatin.

2. Materials and methods

2.1. Preparation and evaluation of decellularized lung scaffolds

Male Bama miniature pigs weighing 30–40 kg were purchased from Sainuo Biomedical (Chengdu, China). All animal protocols were performed in accordance with the guidelines of the Laboratory Animal Welfare Act and standard operating procedures at the Sichuan University Research Center with the approvals of the Animal Experiment Center of Sichuan University. Animals were anesthetized with Zoletil 50 (10 mg/kg body weight, Virbac, France) and maintained with propofol (6 mg/kg/h, Qingyuan Jiabo, China). The lungs were excised, the pulmonary artery and bronchus of the porcine lungs were cannulated, and the lungs were rinsed with phosphate-buffered saline (PBS) for 10 min and then stored at −20°C for further decellularization as reported previously [22]. In brief, the lungs were thawed and perfused with double-distilled water (ddH_2O), 0.2% dextrose (Sigma–Aldrich, MO, USA), 1% Triton X-100 (Biofroxx, Einhausen, Germany), and 1% sodium lauryl ether sulfate (SLES) (Biofroxx) at a rate of 100 mL/min. This was followed by 1% Triton X-100 to remove residual SLES. Subsequently, the lungs were washed with ddH_2O to remove residual detergent. As a control group, the lungs were perfused with distilled water only.

Native or decellularized lung scaffold samples were fixed with 4% neutral formalin, and then the sections were stained with hematoxylin and eosin (H&E), Masson's trichrome (MT, G1340, Solarbio, Beijing, China), and Gomori's aldehyde fuchsin (GAF, G1593, Solarbio) according to established protocols. Images were captured on a NanoZoomer Digital Pathology (NDP) scanning system (Hamamatsu, Hamamatsu City, Japan). In addition, primary antibodies against collagen-IV (ab6586, 1:500, Abcam, MA, USA), fibronectin (ab6328, 1:200, Abcam), and laminin (ab11575, 1:200, Abcam) were used to determine the retention of crucial proteins in the lung. The images were captured using an N-SIM-S Super Resolution Microscope (Nikon, Tokyo, Japan). The morphology of the ECM was also determined by scanning electron microscopy (SEM). Electron micrographs of lung cross-sections were obtained at 5.0×kV and 600 × magnification using a Hitachi S-4800 SEM (Hitachi, Tokyo, Japan).

Total DNA from native and decellularized tissues (10 mg dry weight) was extracted with a Tissue DNaeasy Kit (Tiangen Biotech, Beijing, China) and quantified using a NanoDrop One spectrophotometer (Thermo, MA, USA). Sulfated glycosaminoglycans (GAGs) were quantified using the Blyscan GAG assay kit (Biocolor, Belfast, UK). After incubation with the Blyscan dye reagent and centrifugation, the samples were quantified by measuring the absorbance at 650 nm.

2.2. Preparation of the dECM hydrogel

The dECM hydrogel was prepared as described with modifications [23–25]. After decellularization, the lungs were cut into 1 × 1 × 1 cm diameter disks for lyophilization. Lyophilized lung scaffolds were ground using a Wiley Mill (Retsch, MM400, Haan, Germany) and filtered through an 80 mesh screen. The 1 g ground lung scaffold was then enzymatically digested in 50 mL of 2 g/L porcine pepsin (Sigma–Aldrich) in 0.01 M HCl at a 60 rpm stirring rate for 48 h at 25°C. The lung dECM hydrogel was neutralized to a pH of 7.2–7.4 with 0.1 M NaOH to terminate the pepsin activity. Then, the neutralized lung dECM hydrogel was diluted with 10 × PBS at a ratio of 9:1 (v/v), and the concentration of dECM was adjusted to 10 g/L using 1 × PBS and stored at 4°C for further use. All procedures were performed on ice. The protein concentration of the dECM hydrogel was measured using a NanoDrop spectrophotometer at 280 nm (ND-2000c; Thermo, USA).

2.3. Cell culture

Human lung cancer A549 and H1299 cells were cultured in high-glucose Dulbecco's modified Eagle's medium (DMEM, HyClone, MA, USA) containing 10% fetal bovine serum (Gibco, NY, USA) and 1% penicillin–streptomycin solution (HyClone) in an incubator at 37°C under 5% CO_2 with saturated humidity. The medium was changed three times per week.

2.4. Plate coating and characteristics evaluation

The dECM hydrogel was diluted to a concentration of 0.1 g/L with PBS, and collagen I (BD Biosciences, MA, USA) and Matrigel (Corning, MA, USA) at the same concentration were used as positive coating controls. Five hundred microliters of coating hydrogel was added to 24-well cell culture plates and then placed into a 37°C incubator for 1 h. The excess liquid was discarded, and the plates were washed with PBS. Uncoated plates were used as a negative control. The plates were seeded with A549 or H1299 cells, and nonadherent cells were counted after 4 h of culture using a Countess™ II FL Automated Cell Counter (Invitrogen, CA, USA). The plates were cultured in an incubator at 37°C under 5% CO_2 with saturated humidity. The viability of cells at 1, 3 and 5 days was

assessed using FluoroQuench fluorescent stain (One Lambda, CA, USA) according to the manufacturer's protocol. Representative samples were imaged using a fluorescence microscope (Axio Observer D1/AX10 cam HRC, Carl Zeiss, Gttingen, Germany). The Cell Counting Kit-8 (CCK-8, MCE, NJ, USA) assay was performed in a 96-well plate and measured using a NanoDrop spectrophotometer at 450 nm to quantify cell proliferation capacity.

2.5. Label-free LC–MS/MS proteomic analysis of the dECM hydrogel

dECM samples were lysed, and proteins were extracted and digested. The molecular weight of the dECM hydrogel was determined by sodium dodecyl sulfate (SDS) - polyacrylamide gel electrophoresis (PAGE) according to the manufacturer's instructions.

LC–MS/MS analysis was performed on a timsTOF Pro mass spectrometer (Bruker) coupled to Nanoelute (Bruker Daltonics). The raw MS data for each sample were combined and searched using MaxQuant 1.5.3.17 software for identification and quantitation analysis. The bioinformatic analysis was performed and visualized.

2.6. Micropattern array printing

Polydimethylsiloxane (PDMS) seals were made using a laser etching characteristic pattern silicon wafer as a template as reported previously [26]. A 20 × 20 mm^2 PDMS substrate consists of round patterns with a diameter of 50, 100, 150 or 200 μm and an interspace of 50 μm. The dECM hydrogel was filtered and sterilized, and the entire process was performed aseptically. The PDMS seals were coated with 0.1 g/L dECM hydrogel with 20 μg/mL fluorescein isothiocyanate isomer (FITC, Sigma) for 20 min at room temperature. The PDMS seals were removed, and the dECM hydrogel was dried at 37°C for 10 min. The coated PDMS seals were then placed on a 35-mm nontreated cell culture dish under 0.2 N pressure for 10 min. The morphology of the FITC-labeled microarray was observed using a fluorescence microscope. The printed dishes were stored at room temperature for further use. Before seeding the cells, the printed dishes were incubated with 10 g/L pluronic F-127 solution (Sigma–Aldrich) for 1 h to prevent nonspecific cellular adherence. The culture dishes were sterilized by ultraviolet irradiation for 1 h.

2.7. Spheroid culture

A549 or H1299 cells were suspended in 3 ml medium at a density of 1 × 10^5 cells/ml and inoculated into dECM-printed dishes. The culture medium was removed after 6 h of incubation, and the printed dishes were washed with PBS to remove the unattached cells. In culture, 2.5 mL medium was added to the dish for spheroid culture and changed every other day. As a control group, monolayer cells were cultured under the same conditions. The spheroids and monolayer cells were all cultured in an incubator at 37°C under 5% CO_2 with saturated humidity. The morphology of spheroids was observed using EVOS TM XL Core (Invitrogen) at 6 h and every day after seeding. The diameters of spheroids were analyzed via ImageJ software. The viability of cell spheroids was assessed using FluoroQuench fluorescence viability stain according to the manufacturer's protocol. Cytoplasmic actin microfilament systems were localized using rhodamine-phalloidin (PHDR1, 100 nM, Cytoskeleton, CA, USA) for 45 min at room temperature. Representative samples were imaged by confocal microscopy (Nikon).

2.8. Quantitative real-time polymerase chain reaction (qRT–PCR)

RNA was extracted from cell spheroids at each time point using an RNeasy Mini Kit (Qiagen, CA, USA) according to the manufacturer's instructions. Total RNA (1.0 μg) was reverse-transcribed to complementary DNA (cDNA) using an iScript cDNA Synthesis Kit (Bio–Rad, CA, USA). qRT-PCRs were carried out using iTaq Universal SYBR Green Supermix (Bio–Rad) according to the manufacturer's instructions. The glyceraldehyde-3-phosphate dehydrogenase (GAPDH) housekeeping gene was used as an endogenous internal control, and the results were normalized using the $2^{-\Delta\Delta Ct}$ method (for promoter sequences, Table S1).

2.9. Chemotherapeutic drug cytotoxicity screening

To evaluate the sensitivity of cells to antitumor drugs, A549 or H1299 cells were inoculated into dECM-printed dishes as testing platforms for drug screening. After three days of culture, cell spheroids were incubated with paclitaxel (CSN19486, CSNpharm, IL, USA), doxorubicin (CSN16255, CSNpharm) and cisplatin (HY-17394, MCE) at concentrations of 5 mg/L, 10 mg/L, 50 mg/L and 100 mg/L for 24 h and 48 h, and DMSO (Sigma–Aldrich) and deionized water served as negative control. The morphology of the cell spheroids was observed and imaged. The viability of cell spheroids was assessed using FluoroQuench fluorescent stain and imaged.

2.10. Features of spheroids on dECM-coated micropattern arrays

Relative changes in proliferative ability, physioxia, anti-apoptosis, drug resistance and intracellular pH levels were measured.

Monolayer cells or spheroids were fixed with 4% neutral formalin and then stained with primary antibodies against Ki-67 (ab16667, 1:100, Abcam), HIF-1α (ab1, 1:100, Abcam), MCL-1 (ab32087, 1:100, Abcam), and MRP2 (ab172630, 1:100, Abcam) to determine their characteristics.

Cytosolic pH was measured using the fluorescent dye probe Protonex™ Red 600 (Cat# 21,207, 1 μM; AAT Bioquest) following the manufacturer's instructions. Monolayer cells or spheroids were incubated at 37°C for 30 min. Cells were then gently washed in Hanks solution with 20 mM HEPES and analyzed.

In addition, monolayer cells or spheroids were also stained with N-cadherin (66219-1-Ig, 1:100, Proteintech), β-catenin (ab32572, 1:250, Abcam), and cytokeratin 7 (ab181598, 1:100, Abcam) to determine cell adhesion and interaction.

2.11. Statistics

All data were analyzed with SPSS software version 25 and organized using GraphPad Prism 8. Statistical analysis was performed using one-way ANOVA and Dunnett's post-hoc test. A level of $p < 0.05$ was accepted as significant. At least three parallel experiments were conducted using different samples. Data are presented as the mean ± SEM.

3. Results

3.1. Characterization of decellularized lung scaffold

Visual inspection, as shown in Fig. 1A, revealed that the detergents produced white and translucent lung scaffolds after perfusion. SEM images of the decellularized tissue showed that the ultrastructure of the ECM was preserved and that the cells were successfully removed after decellularization (Fig. 1B). H&E staining confirmed that SLES removed all visible cell components in the proximal and distal lung and bronchus. No cell debris or genetic material was observed in any decellularized group (Fig. 1C). The architecture of the lung and bronchus was preserved after decellularization, as shown by MT, GAF and AB-PAS staining (Fig. 1D–E, Figure S1). Immunofluorescence staining confirmed the removal of cell nuclei and demonstrated the retention of crucial ECM proteins, including collagen IV, fibronectin and laminin (Fig. 1F–H). The level of residual DNA in tissue indicated the removal of cellular material (Fig. 1I). Meanwhile, there was a reduction in GAGs in the decellularized lung scaffolds, but it was not significant (Fig. 1J).

3.2. Characteristics evaluation of dECM-coated plates

The decellularized lungs were lyophilized and ground (Fig. 2A). The

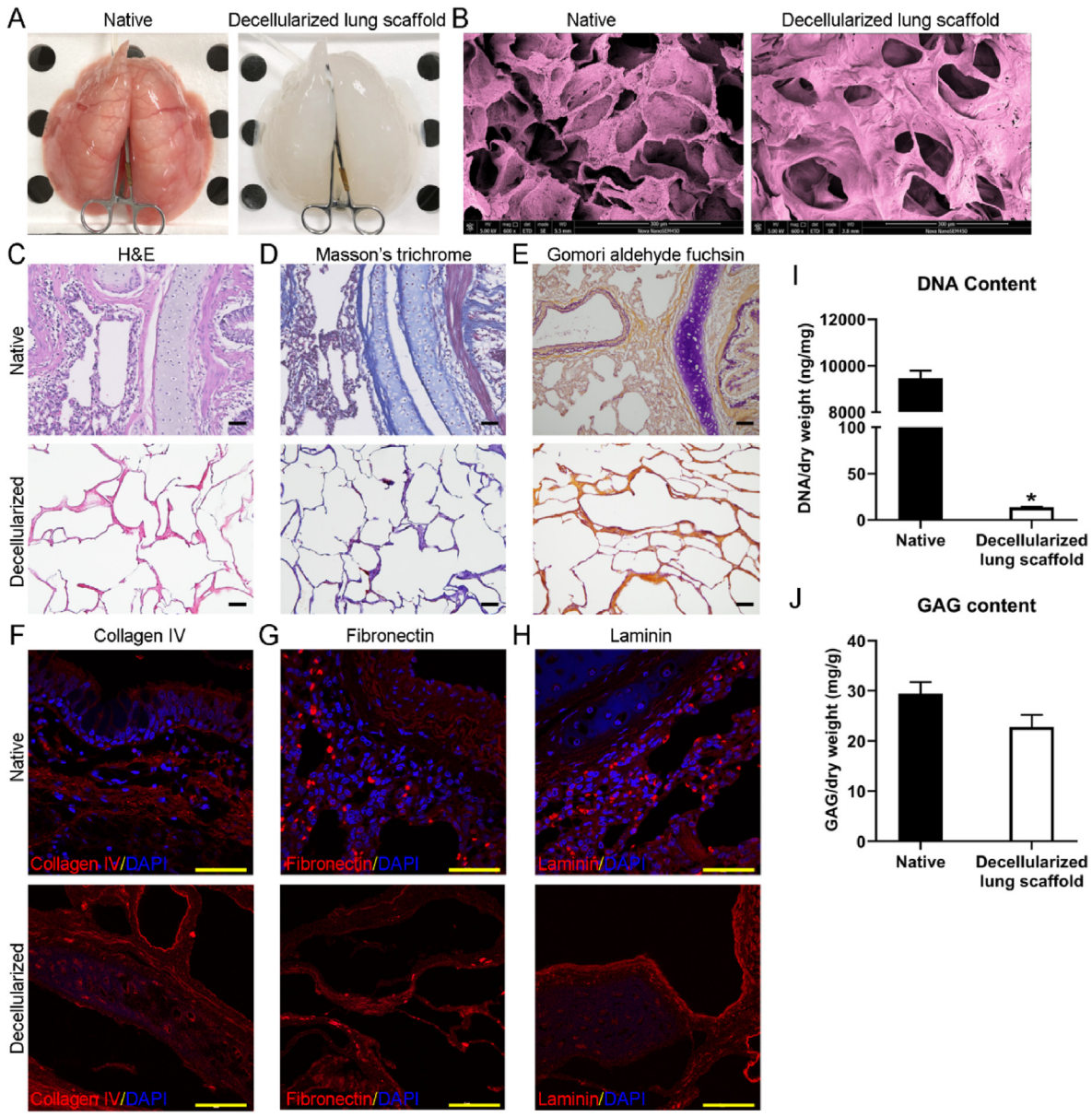

Fig. 1. Morphology of the decellularized lung scaffolds. (A) Macroscopic view of native and decellularized lung scaffolds. (B) SEM images of native lung and decellularized lung scaffolds. (C) H&E, (D) Masson's trichrome and (E) Gomori aldehyde fuchsin staining of native lung and decellularized lung scaffolds. (F) Collagen IV, (G) Fibronectin and (H) Laminin immunofluorescence staining of native lung and decellularized lung scaffolds. (I) Relative DNA content in native lung and decellularized lung scaffolds. (J) Sulfated glycosaminoglycan (GAG) content in native lung and decellularized lung scaffolds. *$p < 0.05$ versus the native group. Scale bar = 50 μm.

powder was then digested by pepsin to form the dECM hydrogel (Fig. 2B). To evaluate attachment capacity, the plates were seeded with A549 or H1299 cells. The number of adherent cells on the dECM-coated plates was greater than that on the uncoated, collagen I or Matrigel-coated plates in both A549 and H1299 cells after 4 h of culture (Fig. 2C–D). The proliferation of H1299 cells cultured on the dECM-coated plates was highest, whereas in A549 cells, the proliferation on the dECM-coated plates was higher than that on the uncoated and collagen I-coated plates, close to Matrigel without statistical significance (Fig. 2E–F). Cells were more evenly distributed and spread out without cavities on the dECM- and Matrigel-coated plates than uncoated and collagen I-coated plates, suggesting strong adhesion (Fig. 2G–H). In addition, the viabilities of both cell types were higher on the dECM-coated plates (Fig. 2G–J).

3.3. Distribution and composition of the dECM

The molecular weights of the dECM hydrogel were evaluated using SDS-PAGE, and the results showed the consistency of components and repeatability of the dECM hydrogel (Fig. 3A). Label-free protein quantification by LC–MS/MS not only allows relative comparison of proteins across samples but also allows estimation of absolute amounts. Using this approach, we analyzed dECM hydrogels derived from decellularized porcine lungs and quantified and identified over 200 core structural components in porcine dECM. We ranked the relative abundance of core matrisome proteins, providing an in-depth dECM expression profile of healthy porcine lungs. Porcine dECM is enriched in glycoproteins, collagens and laminins such as fibrilin-1, collagen 1a1, 1a2 and 6a3, and laminin gamma 1. The dECM also holds receptors and serves as a reservoir for a large number of secreted proteins, such as growth factors. In addition, the components of dECM-modifying enzymes and other dECM-

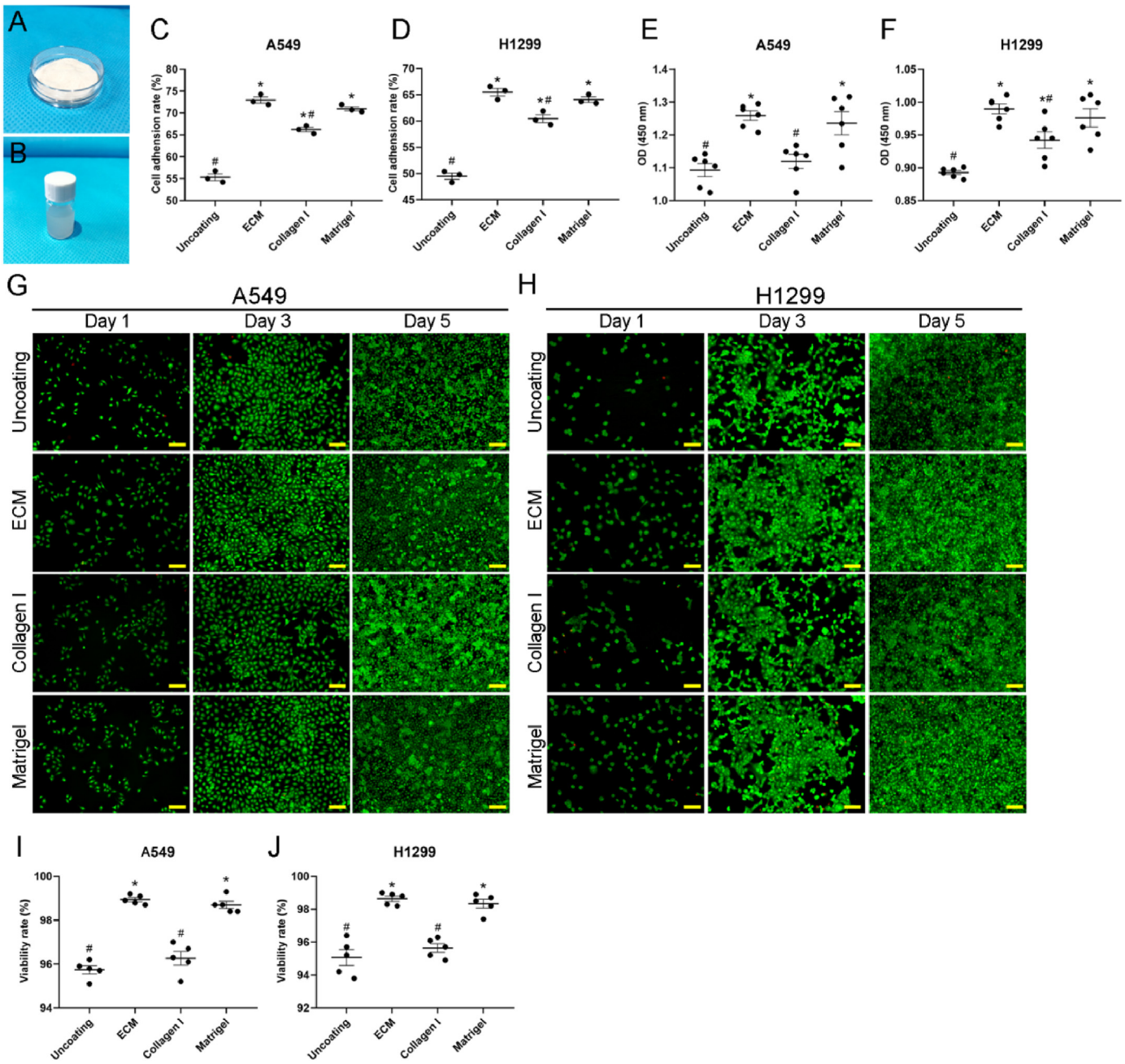

Fig. 2. Preparation and characteristics of extracellular matrix hydrogels derived from decellularized lung scaffolds. (A) Extracellular matrix powder. (B) Extracellular matrix hydrogel. The cell adhesion rate of (C) A549 and (D) H1299 cell lines on extracellular matrix hydrogel at 4 h after cell seeding. The proliferation rate of (E) A549 and (F) H1299 cell line extracellular matrix hydrogels at 24 h after cell seeding. Live/dead staining of (G) A549 and (H) H1299 cell lines cultured on extracellular matrix hydrogel on days 1, 3 and 5. Quantification of viability of (I) A549 and (J) H1299 cell lines cultured on extracellular matrix hydrogel. $*p < 0.05$ versus the uncoated group. $\#p < 0.05$ versus the ECM group. Scale bar = 100 μm.

associated proteins, which, although they do not contribute to the structure of the dECM, affect their functionality as an instructing "niche" (Fig. 3B). The KEGG analyses revealed that significantly enriched pathways were "Focal adhesion", "Regulation of actin cytoskeleton" and "Tight junction" in "Cell motility" and "Cellular community" (Fig. 3C).

3.4. Characteristics of the micropattern array

As shown in Fig. 4A–B, uniformly round micropattern arrays of 50, 100, 150, and 200 μm on dishes was created by the PDMS seals using dECM hydrogel in bright field and fluorescence light. A549 and H1299 cells were seeded on the dECM-coated micropattern array to assess their ability to support cell growth. After 6 h of attachment, the attached cells formed monolayer cells on the micropattern array (Fig. 4C and F). Thereafter, size-controlled and regularly arranged cell spheroids were formed and grew with prolonged culture time (Fig. 4D and G). On day 3, the cell spheroids remained separated. The diameters of the A549 spheroids were 73.6 ± 8.5, 109.2 ± 3.6, 162.4 ± 2.7, and 220.2 ± 5.0 μm (Fig. 4D), while those of the H1299 spheroids at 50, 100, 150 and 200 μm were 63.9 ± 7.2 μm, 97.4 ± 3.7 μm, 144.6 ± 8.2 μm and 194.7 ± 6.5 μm, respectively (Fig. 4G). However, the cell spheroids grew larger and connected each other afterwards (Figure S3). The initial seeding number

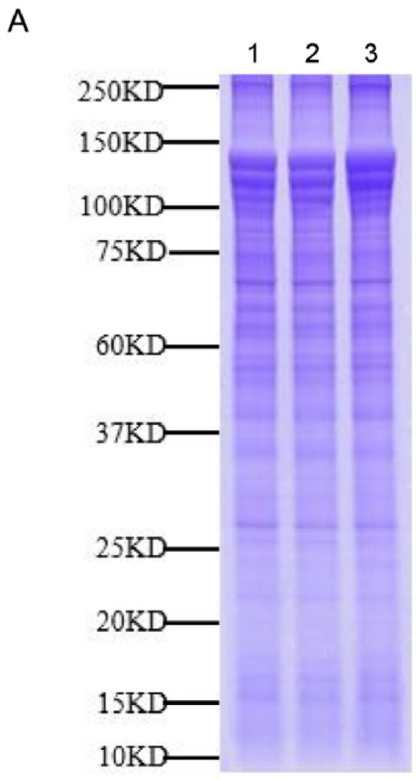

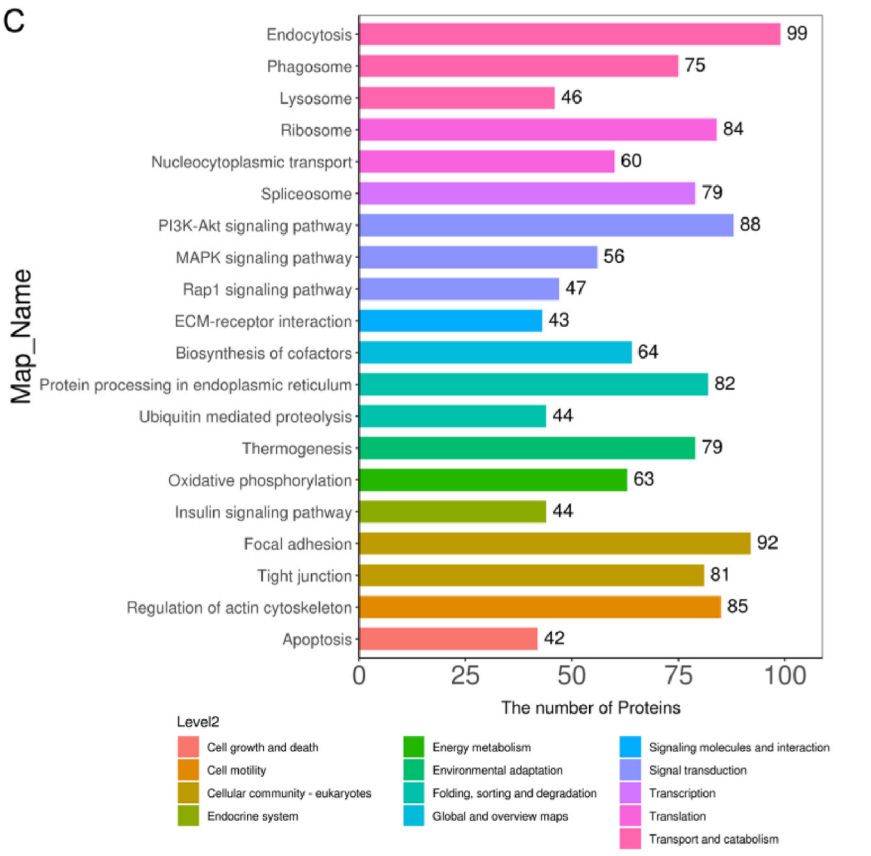

B

Collagens

Gene name	LFQ (log10)	Protein name
COL1A1	7.71	Collagen type I alpha 1 chain
COL1A2	7.32	Fibrillar collagen NC1 domain-containing protein
COL6A3	6.99	Collagen alpha-3(VI) chain isoform 4
COL2A	6.48	Fibrillar collagen NC1 domain-containing protein
COL3A1	6.36	Collagen type III alpha 1 chain
COL4A	6.23	Collagen IV NC1 domain-containing protein
COLGALT1	6.02	Collagen beta(1-O)galactosyltransferase 1
COL6A5	5.65	Collagen type VI alpha 5 chain
COL12A1	5.28	Collagen type XII alpha 1 chain
COL4A6	5.23	Collagen alpha-6(IV) chain isoform 3
COL2A	5.14	Fibrillar collagen NC1 domain-containing protein
COL6A1	5.05	Collagen type VI alpha 1 chain
COL4A1	4.97	Collagen alpha-1(IV) chain isoform 1 preproprotein
PLOD2	4.96	Procollagen-lysine 5-dioxygenase (Fragment)
COL14A1	4.93	Collagen alpha-1(XIV) chain isoform X2
COL11A1	4.76	Collagen type XI alpha 1 chain
COL27A1	4.44	Collagen type XXVII alpha 1 chain
P3H1	4.28	Procollagen-proline 3-dioxygenase
PLOD1	4.08	Procollagen-lysine 5-dioxygenase
P4HA	3.85	Procollagen-proline 4-dioxygenase
COL15A	3.79	Collagen alpha-1(XV) chain
COL5A1	3.79	Fibrillar collagen NC1 domain-containing protein
PLOD3	3.61	Procollagen-lysine 5-dioxygenase
CTHRC1	3.23	Collagen triple helix repeat containing 1
COL11A2	3.04	Collagen type XI alpha 2
COL18A1	Identified	Collagen type XVIII alpha 1 chain
PCOLCE	Identified	Procollagen C-endopeptidase enhancer 1

Laminins

Gene name	LFQ (log10)	Protein name
LAMC1	6.97	Laminin subunit gamma 1
LAMA5	6.25	Laminin subunit alpha-5
LAMB1	6.11	Laminin subunit beta-1
LAMB2	5.71	Laminin subunit beta 2
LAMA3	5.42	Laminin subunit alpha 3
LMNA	5.10	Prelamin-A/C
LMNB2	4.60	Lamin B2
LAMB3	4.59	Laminin subunit beta-3
LAMC2	4.24	Laminin subunit gamma 2
LAMA1	4.19	Laminin subunit alpha-1 isoform X2
LMNB1	3.93	Lamin B1
LMNC	Identified	Lamin isoform C

Integrins

Gene name	LFQ (log10)	Protein name
ITGA6	4.29	Integrin subunit alpha 6
ITGB3	4.21	Integrin beta
ITGAV	4.16	Integrin_alpha2 domain-containing protein
ITGB1	3.92	Integrin beta
ITGA3	3.48	Integrin alpha-3 preproprotein
CD47	Identified	Integrin-associated protein
ILK	Identified	Integrin-linked protein kinase
ITGA5	Identified	Integrin subunit alpha 5
ITGA2	Identified	Integrin subunit alpha 2

Growth factors and receptors

Gene name	LFQ (log10)	Protein name
LTBP2	5.76	Latent transforming growth factor beta binding protein 2
LTBP4	5.53	Latent transforming growth factor beta binding protein 4
IGF2BP3	5.14	Insulin like growth factor 2 mRNA binding protein 3
TGFB1I1	5.05	Transforming growth factor beta 1 induced transcript 1
M6P/IGF2R	4.58	Mannose-6-phosphate/insulin-like growth factor II receptor (
IGFBP4	4.45	Insulin-like growth factor-binding protein 4
TGFBI	4.38	Transforming growth factor-beta-induced protein ig-h3
IGF2BP2	4.30	Insulin like growth factor 2 mRNA binding protein 2
HGFAC	4.24	HGF activator
MST1	4.03	Hepatocyte growth factor-like protein
OGFR	3.69	Opioid growth factor receptor
HDGF	3.66	Heparin binding growth factor
IGF2	Identified	Insulin-like-growth factor 2 preproprotein (Fragment)
IGFBP2	Identified	Insulin-like growth factor-binding protein 2
HGS	Identified	Hepatocyte growth factor-regulated tyrosine kinase substrat
EPS15L1	Identified	Epidermal growth factor receptor substrate 15-like 1 isoform
LTBP1	Identified	Latent transforming growth factor beta binding protein 1
FGF2	Identified	Fibroblast growth factor (Fragment)
PDGFRB	Identified	Platelet-derived growth factor receptor beta (Fragment)
IGFBP6	Identified	Insulin like growth factor binding protein 6
OGFR	Identified	Opioid growth factor receptor (Fragment)
FGFR2	Identified	Keratinocyte growth factor receptor short isoform (Fragmen
GRB2	Identified	Growth factor receptor bound protein 2
IGF2R	Identified	Insulin-like growth factor 2 receptor
MEGF10	Identified	Multiple EGF like domains 10
HDGFL3	Identified	Heparin binding growth factor like 3
MYDGF	Identified	Myeloid derived growth factor

ECM Proteoglycans

Gene name	LFQ (log10)	Protein name
HSPG2	6.08	Basement membrane-specific heparan sulfate proteoglycan
CHAD	5.41	Chondroadherin
OGN	5.27	Mimecan
PRELP	4.93	Prolargin
BGN	4.88	Biglycan (Fragments)
ASPN	4.84	Asporin
PYGM	4.72	Alpha-1,4 glucan phosphorylase
DCN	4.59	Decorin
AGL	4.46	4-alpha-glucanotransferase
HAPLN1	4.34	Hyaluronan and proteoglycan link protein 1
FMOD	4.24	Fibromodulin
GBE1	4.19	1,4-alpha-glucan branching enzyme
PYG	4.02	Alpha-1,4 glucan phosphorylase
PRG4	3.73	Proteoglycan 4
PYGL	3.55	Alpha-1,4 glucan phosphorylase
DAG1	Identified	Alpha-dystroglycan
NMT1	Identified	Glycylpeptide N-tetradecanoyltransferase
NGLY1	Identified	N-glycanase 1
ACAN	Identified	Aggrecan G2 domain (Fragment)
PIGS	Identified	Phosphatidylinositol glycan anchor biosynthesis class S
PIGU	Identified	Phosphatidylinositol glycan anchor biosynthesis class U
PODN	Identified	Podocan
OMD	Identified	Osteomodulin

ECM Glycoproteins

Gene name	LFQ (log10)	Protein name
FBN1	7.83	Fibrillin-1
MFGE8	6.19	Lactadherin
FGB	6.18	Fibrinogen beta chain
THBS1	5.96	Thrombospondin 1
NPNT	5.90	Nephronectin
FN1	5.86	Fibronectin
LTBP2	5.76	Latent transforming growth factor beta binding protein 2
FBN2	5.72	Fibrillin-2
FGG	5.67	Fibrinogen gamma chain
LTBP4	5.53	Latent transforming growth factor beta binding protein 4
DDX17	5.38	DEAD box protein 17
MFAP4	5.37	Fibrinogen C-terminal domain-containing protein
MATN3	5.25	Matrilin 3
VWF	5.16	von Willebrand factor (Fragment)
DDX39B	5.14	DEAD box protein 39B
EFEMP1	5.12	EGF-containing fibulin-like extracellular matrix protein 1
DDX6	5.07	DEAD box protein 6
MATN1	4.96	Matrilin 1
SPARCL1	4.77	SPARC like 1
DDX3X	4.72	DEAD box protein 3X
TINAGL1	4.62	Tubulointerstitial nephritis antigen like 1
FNDC3B	4.59	Fibronectin type III domain containing 3B
FGA	4.57	Fibrinogen alpha chain
DDX58	4.51	DEAD box protein 58
TNC	4.50	Tenascin
FBLN5	4.46	Fibulin-5
DDX52	4.42	DEAD box protein 52
FBLN2	4.32	Fibulin-2
DDX5	4.30	DEAD box protein 5
DDX21	3.63	DEAD box protein 21
THBS4	3.48	Thrombospondin 4
SPARC	3.33	SPARC
ADIPOQ	Identified	Adiponectin (Fragment)
AGRN	Identified	Agrin
COMP	Identified	Cartilage oligomeric matrix protein
DDX10	Identified	DEAD box protein 10
DDX18	Identified	DEAD box protein 18
DDX19B	Identified	DEAD box protein 19B
DDX24	Identified	DEAD box protein 24
DDX46	Identified	DEAD box protein 46
DDX56	Identified	DEAD box protein 56
FGC	Identified	Fibrinogen C-terminal domain-containing protein
LTBP1	Identified	Latent transforming growth factor beta binding protein 1
NID2	Identified	Nidogen-2
POSTN	Identified	Periostin
SPP1	Identified	Osteopontin
VWA5A	Identified	von Willebrand factor A domain containing 5A

Fig. 3. Composition of the ECM. (A) The molecular weights and distributions of the dECM hydrogel were evaluated using SDS-PAGE. (B) Porcine ECM is enriched in glycoproteins, collagens, laminins, proteoglycans, growth factors and receptors, and integrins. (C) KEGG analysis of porcine ECM.

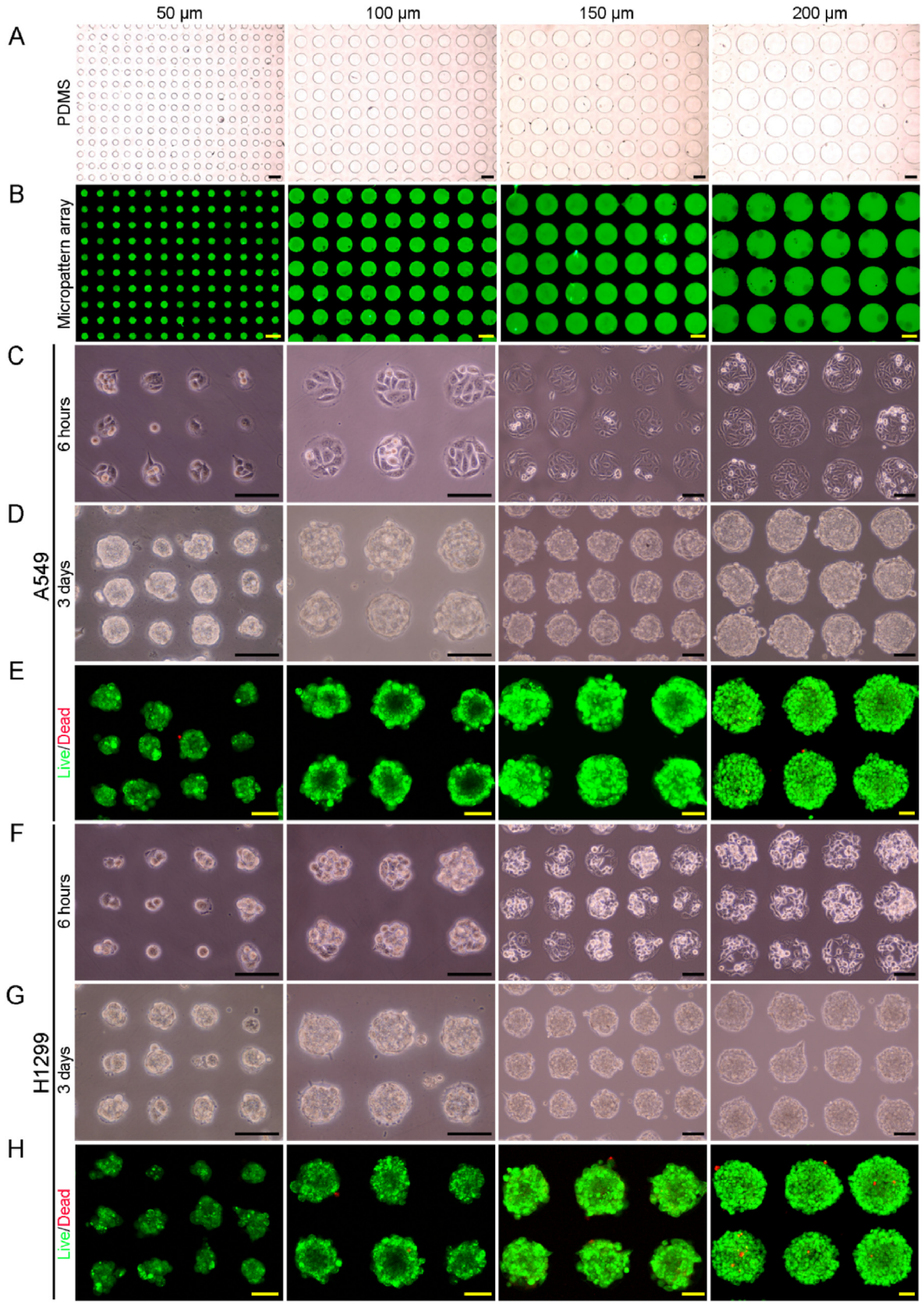

Fig. 4. Fabrication of micropattern arrays and the formation of cancer cell spheroids. Micropattern arrays (A) in bright field and (B) fluorescence light derived from PDMS seals of different diameters (50, 100, 150, 200 μm). (C) A549 cell line cultured on micropattern arrays at 6 h after cell seeding. (D) The A549 cell line formed cancer cell spheroids at day 3 after cell seeding. (E) Live/dead staining of A549 cancer cell spheroids. (F) H1299 cell line cultured on micropattern arrays at 6 h after cell seeding. (G) The H1299 cell line formed cancer cell spheroids at day 3 after cell seeding. (H) Live/dead staining of H1299 cancer cell spheroids. Scale bars = 100 μm.

varied greatly, and the arrays were fragile to support long-term culture on the 50 μm pattern, whereas the spheroids tended to crowd and connect early on the 200 μm pattern, suggesting that the optimal diameter of round patterns on PDMS was 100–150 μm (Fig. 4D and G). The viability of both cell spheroids on the 50, 100 and 150 μm micropattern arrays remained greater than 98% over the 3-day culture; however, dead cells were observed in the 200-μm pattern (Fig. 4E and H).

The height of the dECM-coated micropattern with a diameter of 100 μm was analyzed by confocal microscopy. The results showed that the height of the micropattern was 35.6 ± 0.6 μm (Fig. 5A). The 3D architecture of spheroids on the micropattern array showed bell-shaped cell distribution. A 70–80 μm upthrust was caused by the proliferation of cells in the 100-μm pattern (Fig. 5B, Figure S4). We next analyzed the expression of key genes in lung cancer cells and showed that the expression levels of key genes, including *Vimentin*, *N-cadherin*, *E-cadherin*, *Cd133*, *Cd44*, *Aldh*, and *β-actin,* were higher in the 100-μm pattern,

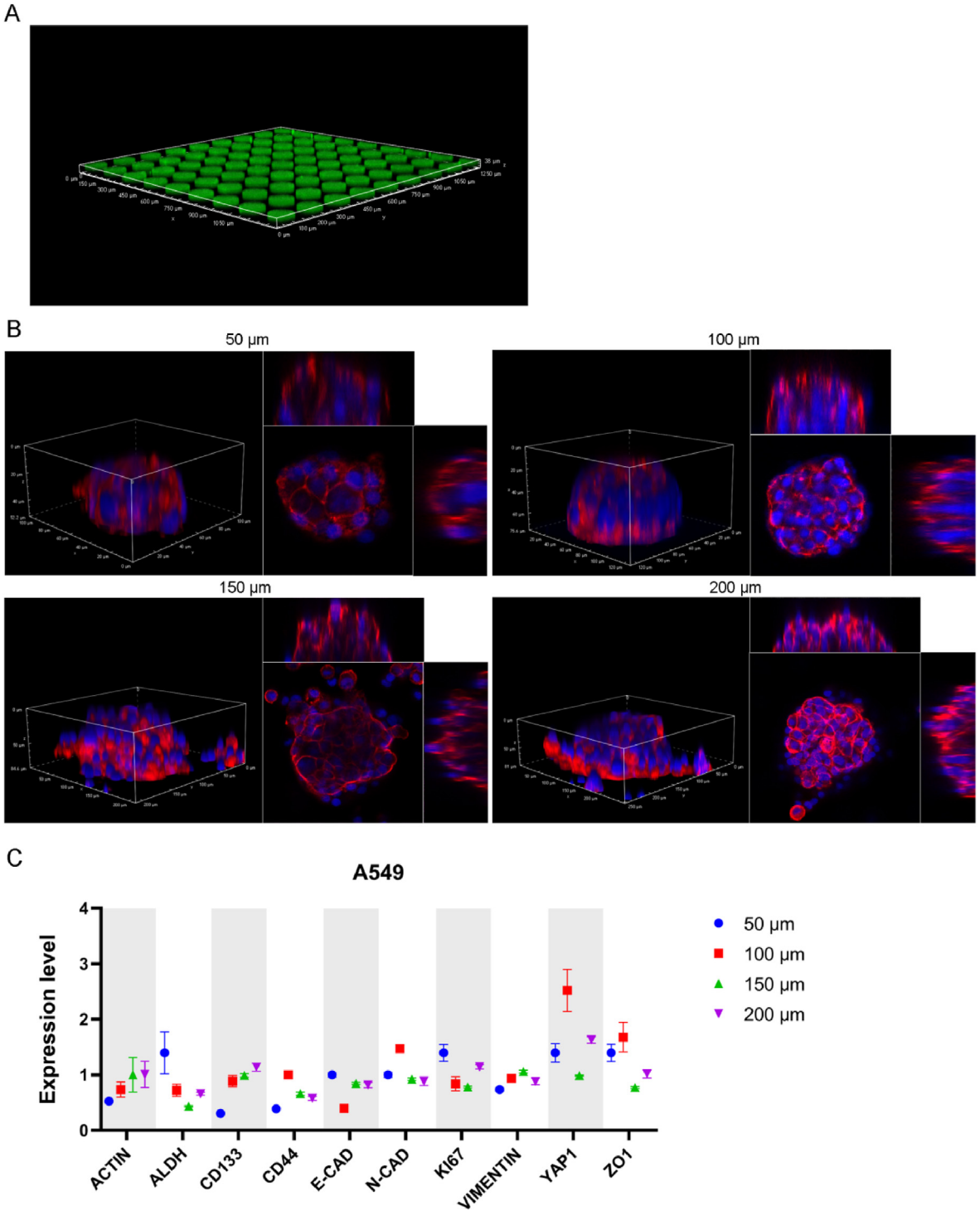

Fig. 5. Characteristics of the micropattern array. (A) The height of the dECM-coated micropattern was analyzed by confocal microscopy. (B) 3D view of A549 cell spheroids in micropattern arrays derived from PDMS seals of different diameters (50, 100, 150, 200 μm). (C) qRT–PCR of A549 cell spheroids in micropattern arrays of different diameters.

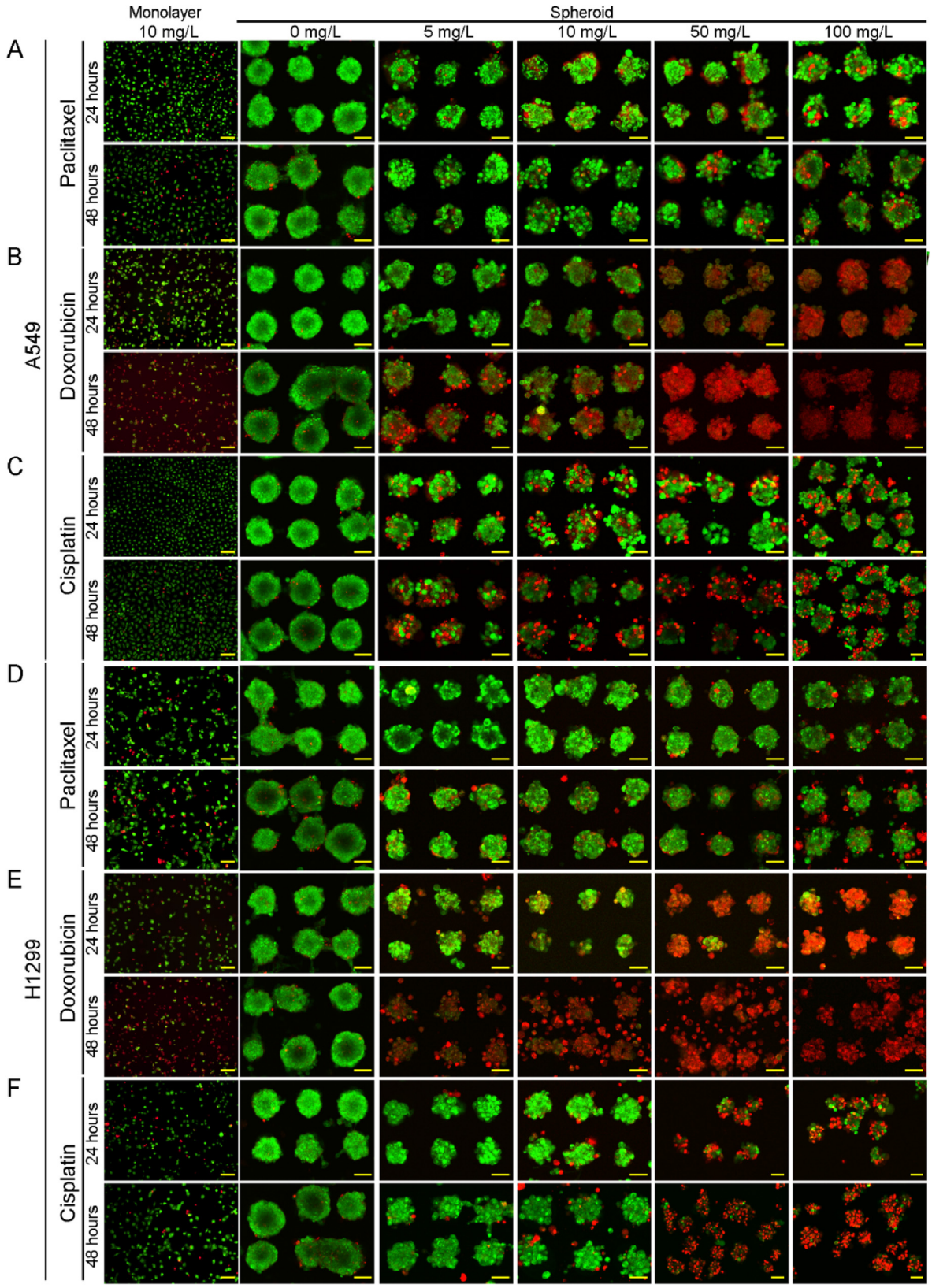

Fig. 6. Drug screening. Drug screening of paclitaxel (A, D), doxorubicin (B, E) and cisplatin (C, F) in A549 and H1299 cells. Scale bars = 100 μm.

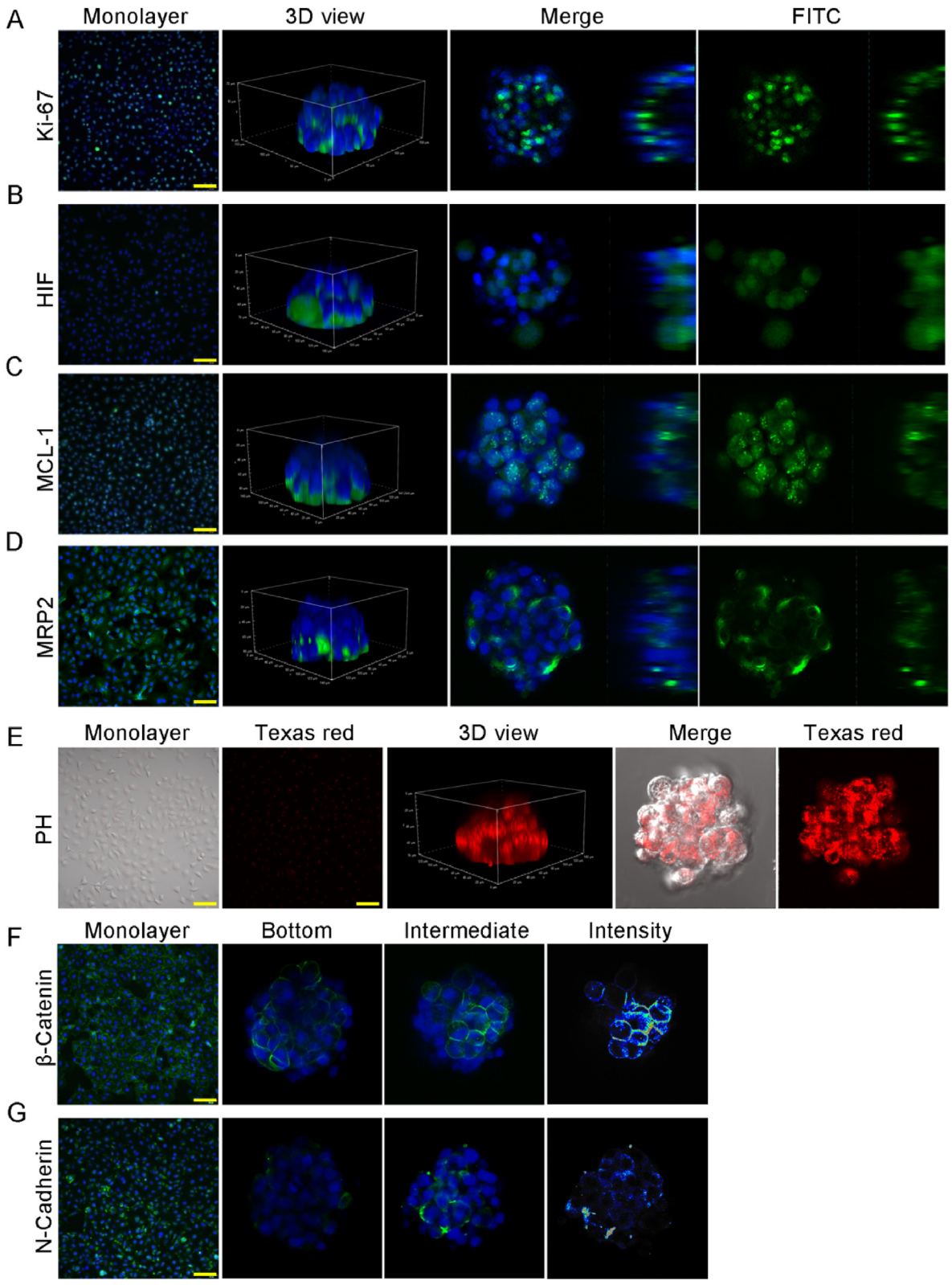

Fig. 7. Features of spheroids on micropattern arrays. Immunofluorescence staining of (A) Ki67 (proliferation marker), (B) HIF-1α (hypoxia marker), (C) MCL-1 (anti-apoptosis marker) and (D) MRP2 (drug resistance) in A549 cell spheroids and monolayers. (E) Cytosolic pH of A549 cell spheroids and monolayers. Immunofluorescence staining of (F) β-catenin and (G) N-cadherin in A549 cell spheroids and monolayers. Scale bars = 100 μm.

followed by the 150-μm pattern (Fig. 5C, Figure S4). The above-mentioned results confirmed that the optimal diameter of the round patterns was 100–150 μm.

3.5. Drug screening

As the consequence, we chose cell spheroids on a 100 μm micropattern array as our candidates for the following drug screening. The cancer cells in spheroids of both A549 and H1299 showed greater resistance to paclitaxel, doxorubicin and cisplatin than monolayer cancer cells. The anticancer drugs at lower concentrations killed more cells; however, in a three-dimensional environment, cancer cell spheroids shrank, and the interior of the spheroids was not completely killed even at high concentrations. The cytotoxic effect of paclitaxel was lower in A549 cells, with survival rates of 92.7%, 85.3%, 70.4%, and 60.2% at 5, 10, 50, and 100 mg/L, respectively (Fig. 6A), while the survival rates of doxorubicin were 58.2%, 50.1%, 1.2%, and 0.0%, respectively (Fig. 6B), and the survival rates of cisplatin were 53.0%, 46.8%, 38.3%, and 31.9% (Fig. 6C) at 48 h after drug administration. In H1299, the survival rates were 88.3%, 84.8%, 68.2%, and 57.6%, respectively (Fig. 6D), while the survival rates of doxorubicin were 4.7%, 3.1%, 0.0%, and 0.0%, respectively (Fig. 6E), and the survival rates of cisplatin were 91.1%, 80.3%, 16.5%, and 10.9% (Fig. 6F) at 48 h after drug administration. As a control group, 0 mg/L anticancer drugs were used to treat cancer spheroids.

3.6. Features of spheroids on micropattern arrays

Immunofluorescence images showed that spheroids had higher expression of Ki67 (proliferation marker), HIF-1α (hypoxia marker), MCL-1 (anti-apoptosis marker) and MRP2 (drug resistance) than monolayer cells (Fig. 7A–D), and the results were confirmed by qRT-PCR (Figure S5). However, the distributions of positive cells were different. The HIF-1α-positive and MCL-1-positive cells were located in the center of the spheroids, while the Ki-67-positive and MRP2-positive cells were spread in the periphery of the spheroids (Fig. 7A–D). The cytosolic pH was lower in the interior than in the periphery, as evidenced by the higher fluorescence intensity of the pH indicator Protonex red (Fig. 7E). In addition, the expression of β-catenin, N-cadherin and cytokeratin 7 was widely enriched in cell–cell interaction regions, indicating the establishment of basal-lateral polarity (Fig. 7F–G, Figure S6).

4. Discussion

In this experiment, we established an ECM-based hydrogel derived from decellularized porcine lungs and then made micropattern arrays using PDMS. The results demonstrated that dECM supported cell adhesion, distribution, viability and proliferation better than collagen I and Matrigel as the coated matrix on the surface. Moreover, we proved that the optimal diameter of the micropattern arrays was 100–150 μm by measuring the morphology, viability, proliferation and phenotype of the cell spheroids. Cell spheroids of A549 and H1299 on dECM-coated micropattern arrays were evaluated for the cytotoxicity of paclitaxel, doxorubicin and cisplatin as a testing platform.

Three-dimensional culture has great potential for preclinical drug screening. Cancer cells grow in three dimensions and can mimic the complexity and heterogeneity of tumors. Cancer spheroids or organoids can maintain their viability, morphology, phenotype, metabolism and function. In addition, dECM can affect cell shape, permeability and rearrangement of the cytoskeleton, thus enhancing cell-matrix interactions and mimicking the ultrastructure and microenvironment *in vivo*. Previous reports revealed that three-dimensional spheroids exhibited more chemoresistance than cells in monolayers due to poor penetration of anticancer drugs into the interior of the sphere [27,28]. Anti-proliferative drugs aimed at dividing cells, such as paclitaxel and cisplatin, showed a reduced effect on anti-apoptotic and quiescent cancer cells in the interior of spheroids. Hypoxia and low pH could also contribute to drug resistance inside spheroids [28,29]. Anticancer drugs such as doxorubicin and epirubicin are designed to generate free radicals, which could be less harmful to DNA in the absence of oxygen. Cancer-associated fibroblasts and macrophages *in vivo* tumors can form a physical barrier to resist [30–32] or even increase drug efflux [33,34]. In contrast, drug resistance can be alleviated when the three-dimensional environment is removed, reflecting that chemoresistance is related to interactions. In our study, monolayer cancer cells were sensitive to lower concentrations of anticancer drugs, indicating that three-dimensional cultures were more resistant than monolayers of both A549 and H1299 cells. Three-dimensional cell culture models pave the way for mimicking the realistic microenvironment of cell–cell and cell-matrix and recapitulating natural three-dimensional tumors.

Collagen, gelatin, fibrin, hyaluronic acid, chitosan and alginate are widely used natural polymeric biomaterials because of their resemblance to native ECM components [35,36]. A well-defined matrix, such as collagen I utilized in our study, can produce limited variability in experimental results and thus is suitable for the study of the function of a single component. Matrigel is a commercialized gelatinous protein mixture extracted from Engelbreth-Holm-Swarm mouse sarcoma. It is rich in laminin, contains collagen IV, heparan sulfate, entactin and a variety of growth factors and is a commonly used system for three-dimensional cell culture research *in vitro*. However, the use of an immortalized mouse cell line has been limited by the large differences in xenogenicity and variability between benign and malignant tumors. For instance, the composition of the ECM can affect epithelial-to-mesenchymal transition, chemosensitivity and invasive progression in cancer cells. According to a report, cancer cells seeded in a laminin-rich matrix showed less invasion and dissemination [37]. In this way, Matrigel cannot be regarded as the first choice. The native ECM, on the other hand, comprises key functional proteins, such as collagens, glycoproteins, glycosaminoglycans, proteoglycans, growth factors, cytokines, proteases and integrins [38,39]. We proved that as the surface coating matrix, dECM-based hydrogels were more conducive to cell adhesion, survival, proliferation, and phenotype exhibition in both A549 and H1299 cells. The dECM-based hydrogel derived from decellularized porcine lungs in our study was found to be stable at room temperature for up to 30 days. In addition, extensive qRT–PCR testing performed on a number of porcine-specific pathogens was negative, including porcine endogenous retrovirus and α-1,3-Gal. The dECM-based hydrogel also showed a neutral pH, transparency, permeability and compatibility with both normal and cancer cell types.

By comparing micropattern arrays at different diameters, we found that the optimal diameter of round patterns was 100–150 μm in the field of viability of cell morphology, viability, proliferation and phenotype exhibition. In the 50-μm pattern, the initiating seeding cells were only 0–3, and the arrays were too fragile to support long-term culture, even though they could grow into spheroids of suitable size. Meanwhile, in the 200-μm pattern, the connection and death of spheroids could occur early. This could be explained by the fact that necrosis occurred in the spheroids because of a lack of oxygen and nutrient diffusion with increasing diameter. Furthermore, enough space should be provided for cell growth rapidly and steadily.

It is shown in the ATCC website (https://www.atcc.org/) that A549 was derived from adenocarcinoma alveolar epithelial cells, while H1299 was established from metastatic lymph nodes, and these two were both non-small-cell lung carcinomas. Furthermore, H1299 is more malignant, notably possessing the P53 deletion mutation [40]. To our knowledge, H1299 cells more easily form tumors in a mouse model than A549 cells. The results of our study showed that H1299 tended to aggregate, proliferate and form spheroids, indicating a more aggressive, more rapid doubling time of tumor volume and higher stemness in H1299 spheroids, consistent with its phenotype. Meanwhile, the results also demonstrated that drug screenings should be performed after spheroid formation rather than at a fixed time after seeding. As previous results confirmed, A549

spheroids had an efficacy of resistance to cisplatin, and H1299 cells showed more sensitivity to cytotoxic anticancer drugs such as cisplatin, etoposide, gemcitabine, vinblastine, taxol, and doxorubicin. In our study, we showed that H1299 cells display a relatively higher sensitivity to doxorubicin and cisplatin treatment and, to a lesser extent, to paclitaxel. Under identical conditions, a 2-day treatment with cisplatin concentrations over 50 mg/L was sufficient to induce extensive cell death of the H1299 cells. However, treatment with cisplatin concentrations as high as 100 mg/L was needed to achieve a similar effect on A549 cells. These results demonstrated that the responses of different sources of cells to a variety of drugs can be compared directly and illustrated the necessity and usefulness of drug screening before therapeutic interventions as genetically distinct individuals.

According to a previous study, spheroids or organoids of cancer cells embedded in matrix showed higher chemoresistance than those cultured on three-dimensional culture or matrix-based culture alone [29]. The advantage of our study lies in the combination of three-dimensional and natural dECM-based culture in the platform. The most immediate application of this study will take place in the field of pharmaceutical development and individualization. Standardization is necessary before immortalized cancer cell lines can be applied in routine pharmacotoxicology. From organ sources and animal age, decellularized reagents and exposure times, to the shape, size and arrangement of cancer spheroids could strongly affect drug efficacy and toxicity [41,42]. The emergence of micropattern arrays will enhance the efficiency and affordability of the novel drug development process. Patient-derived xenografts (PDXs) can be tested in this platform, and their chemosensitivity profiles can be observed. More advanced, primary cancer cells from human patients can be directly seeded to establish patient-derived organoids (PDOs) on our platform and allow for the prediction of interindividual differences in drug sensitivity and metabolism mediated by genetic polymorphisms, including efficacy and adverse reactions. Drug screening in micropattern arrays provides a powerful alternative to existing methods for drug testing and metabolic profiling. The patient-derived *in vitro* cell model will be able to reduce unresponsiveness or undesired outcomes.

Credit author statement

Xinglong Zhu: Investigation Writing – original draft preparation. Yi Li: Investigation Writing- Reviewing and Editing. Ying Yang: Visualization. Yuting He: Investigation, Validation. Mengyu Gao: Investigation, Validation. Wanliu Peng: Validation. Qiong Wu: Resources. Guangyue Zhang: Validation. Yanyan Zhou: Validation. Fei Chen: Visualization. Ji Bao: Conceptualization, Methodology. Weimin Li: Supervision

Funding information

China Postdoctoral Science Foundation, Grant/Award Number: 2018M643504; Post-Doctor Research Project, West China Hospital, Sichuan University, Grant/Award Number: 2018HXBH041.

Data availability statement

The data used to support the findings of this study are available from the corresponding author upon request.

Declaration of competing interest

The authors declare that they have no known competing financial interests or personal relationships that could have appeared to influence the work reported in this paper.

Acknowledgments

The authors are grateful to Ying Yang for their valuable assistance.

Appendix A. Supplementary data

Supplementary data to this article can be found online at https://doi.org/10.1016/j.mtbio.2022.100274.

References

[1] F. Michor, V.M. Weaver, Understanding tissue context influences on intratumour heterogeneity, Nat. Cell Biol. 16 (4) (2014) 301–302, https://doi.org/10.1038/ncb2942.
[2] D. Delle Cave, R. Rizzo, B. Sainz Jr., G. Gigli, L.L. Del Mercato, E. Lonardo, The revolutionary roads to study cell-cell interactions in 3D in vitro pancreatic cancer models, Cancers 13 (4) (2021), https://doi.org/10.3390/cancers13040930.
[3] F. Pampaloni, E.G. Reynaud, E.H. Stelzer, The third dimension bridges the gap between cell culture and live tissue, Nat. Rev. Mol. Cell Biol. 8 (10) (2007) 839–845, https://doi.org/10.1038/nrm2236.
[4] M. Gotte, I. Kovalszky, Extracellular matrix functions in lung cancer, Matrix Biol. 73 (2018) 105–121, https://doi.org/10.1016/j.matbio.2018.02.018.
[5] C. Walker, E. Mojares, A. Del Rio Hernandez, Role of extracellular matrix in development and cancer progression, Int. J. Mol. Sci. 19 (10) (2018), https://doi.org/10.3390/ijms19103028.
[6] L.T. Saldin, M.C. Cramer, S.S. Velankar, L.J. White, S.F. Badylak, Extracellular matrix hydrogels from decellularized tissues: structure and function, Acta Biomater. 49 (2017) 1–15, https://doi.org/10.1016/j.actbio.2016.11.068.
[7] U. Mendibil, R. Ruiz-Hernandez, S. Retegi-Carrion, N. Garcia-Urquia, B. Olalde-Graells, A. Abarrategi, Tissue-specific decellularization methods: rationale and strategies to achieve regenerative compounds, Int. J. Mol. Sci. 21 (15) (2020), https://doi.org/10.3390/ijms21155447.
[8] R.H.J. de Hilster, P.K. Sharma, M.R. Jonker, E.S. White, E.A. Gercama, M. Roobeek, W. Timens, M.C. Harmsen, M.N. Hylkema, J.K. Burgess, Human lung extracellular matrix hydrogels resemble the stiffness and viscoelasticity of native lung tissue, Am. J. Physiol. Lung Cell Mol. Physiol. 318 (4) (2020) L698–l704, https://doi.org/10.1152/ajplung.00451.2019.
[9] B.M. Young, K. Shankar, C.K. Tho, A.R. Pellegrino, R.L. Heise, Laminin-driven Epac/Rap1 regulation of epithelial barriers on decellularized matrix, Acta Biomater. 100 (2019) 223–234, https://doi.org/10.1016/j.actbio.2019.10.009.
[10] S. Park, T.H. Kim, S.H. Kim, S. You, Y. Jung, Three-dimensional vascularized lung cancer-on-a-chip with lung extracellular matrix hydrogels for in vitro screening, Cancers 13 (16) (2021), https://doi.org/10.3390/cancers13163930.
[11] B. Falcones, H. Sanz-Fraile, E. Marhuenda, I. Mendizábal, I. Cabrera-Aguilera, N. Malandain, J.J. Uriarte, I. Almendros, D. Navajas, D.J. Weiss, R. Farré, J. Otero, Bioprintable lung extracellular matrix hydrogel scaffolds for 3D culture of mesenchymal stromal cells, Polymers 13 (14) (2021), https://doi.org/10.3390/polym13142350.
[12] M.M. De Santis, H.N. Alsafadi, S. Tas, D.A. Bölükbas, S. Prithiviraj, I.A.N. Da Silva, M. Mittendorfer, C. Ota, J. Stegmayr, F. Daoud, M. Königshoff, K. Swärd, J.A. Wood, M. Tassieri, P.E. Bourgine, S. Lindstedt, S. Mohlin, D.E. Wagner, Extracellular-matrix-reinforced bioinks for 3D bioprinting human tissue, Adv. Mater. 33 (3) (2021), e2005476, https://doi.org/10.1002/adma.202005476.
[13] J. Zhou, P. Wu, H. Sun, H. Zhou, Y. Zhang, Z. Xiao, Lung tissue extracellular matrix-derived hydrogels protect against radiation-induced lung injury by suppressing epithelial-mesenchymal transition, J. Cell. Physiol. 235 (3) (2020) 2377–2388, https://doi.org/10.1002/jcp.29143.
[14] M. Gomez-Florit, A. Pardo, R.M.A. Domingues, A.L. Graca, P.S. Babo, R.L. Reis, M.E. Gomes, Natural-based hydrogels for tissue engineering applications, Molecules 25 (24) (2020), https://doi.org/10.3390/molecules25245858.
[15] W. Zhang, A. Du, S. Liu, M. Lv, S. Chen, Research progress in decellularized extracellular matrix-derived hydrogels, Regen. Ther. 18 (2021) 88–96, https://doi.org/10.1016/j.reth.2021.04.002.
[16] L. Zhu, C. Shao, H. Chen, Z. Chen, Y. Zhao, Hierarchical hydrogels with ordered micro-nano structures for cancer-on-a-chip construction, Research 2021 (2021) 9845679, https://doi.org/10.34133/2021/9845679.
[17] H. Zhang, J. Guo, Y. Wang, L. Sun, Y. Zhao, Stretchable and conductive composite structural color hydrogel films as bionic electronic skins, Adv. Sci. 8 (20) (2021), e2102156, https://doi.org/10.1002/advs.202102156.
[18] E.T. Verjans, J. Doijen, W. Luyten, B. Landuyt, L. Schoofs, Three-dimensional cell culture models for anticancer drug screening: worth the effort? J. Cell. Physiol. 233 (4) (2018) 2993–3003, https://doi.org/10.1002/jcp.26052.
[19] N. Tanaka, H. Ota, K. Fukumori, J. Miyake, M. Yamato, T. Okano, Micro-patterned cell-sheets fabricated with stamping-force-controlled micro-contact printing, Biomaterials 35 (37) (2014) 9802–9810, https://doi.org/10.1016/j.biomaterials.2014.08.043.
[20] S. Hu, T.H. Chen, Y. Zhao, Z. Wang, R.H.W. Lam, Protein-substrate adhesion in microcontact printing regulates cell behavior, Langmuir 34 (4) (2018) 1750–1759, https://doi.org/10.1021/acs.langmuir.7b02935.

[21] Y. Shen, N. Tanaka, H. Yamazoe, S. Furutani, H. Nagai, T. Kawai, Y. Tanaka, Flow analysis on microcasting with degassed polydimethylsiloxane micro-channels for cell patterning with cross-linked albumin, PLoS One 15 (5) (2020), e0232518, https://doi.org/10.1371/journal.pone.0232518.
[22] Y. Li, Q. Wu, L. Li, F. Chen, J. Bao, W. Li, Decellularization of porcine whole lung to obtain a clinical-scale bioengineered scaffold, J. Biomed. Mater. Res. (2021), https://doi.org/10.1002/jbm.a.37158.
[23] R.A. Pouliot, P.A. Link, N.S. Mikhaiel, M.B. Schneck, M.S. Valentine, F.J. Kamga Gninzeko, J.A. Herbert, M. Sakagami, R.L. Heise, Development and characterization of a naturally derived lung extracellular matrix hydrogel, J. Biomed. Mater. Res. 104 (8) (2016) 1922–1935, https://doi.org/10.1002/jbm.a.35726.
[24] P.A. Link, R.A. Pouliot, N.S. Mikhaiel, B.M. Young, R.L. Heise, Tunable hydrogels from pulmonary extracellular matrix for 3D cell culture, JoVE : JoVE 119 (2017), https://doi.org/10.3791/55094.
[25] R.A. Pouliot, B.M. Young, P.A. Link, H.E. Park, A.R. Kahn, K. Shankar, M.B. Schneck, D.J. Weiss, R.L. Heise, Porcine lung-derived extracellular matrix hydrogel properties are dependent on pepsin digestion time, Tissue Eng. C Methods 26 (6) (2020) 332–346, https://doi.org/10.1089/ten.TEC.2020.0042.
[26] Y. Zhang, M. Gao, M. Hu, B. Zhang, Y. He, S. Li, J. Bao, H. Bu, Using the patterned microarray culture to obtain gene-editing monoclonal cells, Transplant. Proc. 52 (6) (2020) 1906–1909, https://doi.org/10.1016/j.transproceed.2020.02.138.
[27] A.I. Minchinton, I.F. Tannock, Drug penetration in solid tumours, Nat. Rev. Cancer 6 (8) (2006) 583–592, https://doi.org/10.1038/nrc1893.
[28] M.W. Dewhirst, T.W. Secomb, Transport of drugs from blood vessels to tumour tissue, Nat. Rev. Cancer 17 (12) (2017) 738–750, https://doi.org/10.1038/nrc.2017.93.
[29] Y. Jo, N. Choi, K. Kim, H.J. Koo, J. Choi, H.N. Kim, Chemoresistance of cancer cells: requirements of tumor microenvironment-mimicking in vitro models in anti-cancer drug development, Theranostics 8 (19) (2018) 5259–5275, https://doi.org/10.7150/thno.29098.
[30] B. Ruffell, L.M. Coussens, Macrophages and therapeutic resistance in cancer, Cancer Cell 27 (4) (2015) 462–472, https://doi.org/10.1016/j.ccell.2015.02.015.
[31] K.E. Richards, A.E. Zeleniak, M.L. Fishel, J. Wu, L.E. Littlepage, R. Hill, Cancer-associated fibroblast exosomes regulate survival and proliferation of pancreatic cancer cells, Oncogene 36 (13) (2017) 1770–1778, https://doi.org/10.1038/onc.2016.353.
[32] D. Ganguly, R. Chandra, J. Karalis, M. Teke, T. Aguilera, R. Maddipati, M.B. Wachsmann, D. Ghersi, G. Siravegna, H.J. Zeh 3rd, R. Brekken, D.T. Ting, M. Ligorio, Cancer-associated fibroblasts: versatile players in the tumor microenvironment, Cancers 12 (9) (2020), https://doi.org/10.3390/cancers12092652.
[33] M.M. Gottesman, T. Fojo, S.E. Bates, Multidrug resistance in cancer: role of ATP-dependent transporters, Nat. Rev. Cancer 2 (1) (2002) 48–58, https://doi.org/10.1038/nrc706.
[34] R.W. Robey, K.M. Pluchino, M.D. Hall, A.T. Fojo, S.E. Bates, M.M. Gottesman, Revisiting the role of ABC transporters in multidrug-resistant cancer, Nat. Rev. Cancer 18 (7) (2018) 452–464, https://doi.org/10.1038/s41568-018-0005-8.
[35] R. Song, M. Murphy, C. Li, K. Ting, C. Soo, Z. Zheng, Current development of biodegradable polymeric materials for biomedical applications, Drug Des. Dev. Ther. 12 (2018) 3117–3145, https://doi.org/10.2147/DDDT.S165440.
[36] J. Gopinathan, I. Noh, Recent trends in bioinks for 3D printing, Biomater. Res. 22 (2018) 11, https://doi.org/10.1186/s40824-018-0122-1.
[37] G.M. Cramer, D.P. Jones, H. El-Hamidi, J.P. Celli, ECM composition and rheology regulate growth, motility, and response to photodynamic therapy in 3D models of pancreatic ductal adenocarcinoma, Mol. Cancer Res. : MCR 15 (1) (2017) 15–25, https://doi.org/10.1158/1541-7786.mcr-16-0260.
[38] G. Burgstaller, B. Oehrle, M. Gerckens, E.S. White, H.B. Schiller, O. Eickelberg, The instructive extracellular matrix of the lung: basic composition and alterations in chronic lung disease, Eur. Respir. J. 50 (1) (2017), https://doi.org/10.1183/13993003.01805-2016.
[39] Y. Zhou, J.C. Horowitz, A. Naba, N. Ambalavanan, K. Atabai, J. Balestrini, P.B. Bitterman, R.A. Corley, B.S. Ding, A.J. Engler, K.C. Hansen, J.S. Hagood, F. Kheradmand, Q.S. Lin, E. Neptune, L. Niklason, L.A. Ortiz, W.C. Parks, D.J. Tschumperlin, E.S. White, H.A. Chapman, V.J. Thannickal, Extracellular matrix in lung development, homeostasis and disease, Matrix Biol. 73 (2018) 77–104, https://doi.org/10.1016/j.matbio.2018.03.005.
[40] T. Mitsudomi, S.M. Steinberg, M.M. Nau, D. Carbone, D. D'Amico, S. Bodner, H.K. Oie, R.I. Linnoila, J.L. Mulshine, J.D. Minna, et al., p53 gene mutations in non-small-cell lung cancer cell lines and their correlation with the presence of ras mutations and clinical features, Oncogene 7 (1) (1992) 171–180.
[41] D. Choudhury, M. Yee, Z.L.J. Sheng, A. Amirul, M.W. Naing, Decellularization systems and devices: state-of-the-art, Acta Biomater. 115 (2020) 51–59, https://doi.org/10.1016/j.actbio.2020.07.060.
[42] A. Badileanu, C. Mora-Navarro, A.M. Gracioso Martins, M.E. Garcia, D. Sze, E.W. Ozpinar, L. Gaffney, J.R. Enders, R.C. Branski, D.O. Freytes, Fast automated approach for the derivation of acellular extracellular matrix scaffolds from porcine soft tissues, ACS Biomater. Sci. Eng. 6 (7) (2020) 4200–4213, https://doi.org/10.1021/acsbiomaterials.0c00265.